Magnetic Template Anion Polyacrylamide–Polydopamine-Fe$_3$O$_4$ Combined with Ultraviolet/H$_2$O$_2$ for the Rapid Enrichment and Degradation of Diclofenac Sodium from Aqueous Environment

Qiang Sun [1,*] [ID]**, Huaili Zheng** [1,2,*]**, Xuebin Hu** [1,2]**, Jun Li** [1]**, Rui Zhao** [1]**, Chun Zhao** [1,2] **and Wei Ding** [1]

1   Key Laboratory of the Three Gorges Reservoir Region's Eco-Environment, State Ministry of Education, Chongqing University, Chongqing 400045, China; xbhu@cqu.edu.cn (X.H.); ulquiorra_n@163.com (J.L.); 20171713027t@cqu.edu.cn (R.Z.); pureson@163.com (C.Z.); dingweidinghan@163.com (W.D.)
2   State Key Laboratory of Coal Mine Disaster Dynamics and Control, Chongqing University, Chongqing 400044, China
*   Correspondence: 20141913072@cqu.edu.cn (Q.S.); hlz6512@163.com (H.Z.); Tel.: +86-23-65120827 (H.Z.)

✓ check for updates

Abstract: In this study, a novel system was set up by preparing a magnetic flocculant combining with ultraviolet/H$_2$O$_2$ to realize the rapid enrichment and degradation of diclofenac sodium (DCFS). For the magnetic flocculant, template anion polyacrylamide (TAPAM) with anion micro-block structure was prepared. Thereafter, polydopamine was used to modify TAPAM, Fe$_3$O$_4$ nanoparticles was grafted to the modified TAPAM by chelation, named template anion polyacrylamide-polydopamine-Fe$_3$O$_4$ (TAPAM-PDA-Fe$_3$O$_4$). Furthermore, the TAPAM-PDA-Fe$_3$O$_4$ preparation protocol was optimized by the response surface method (RSM). In the DCFS enrichment section, the rapid separation of flocs from water was realized by an external magnetic field and it indicated that the π–π stacking effect was dominant in neutral/alkaline condition, whereas charge neutralization was favored in acidic conditions. Meanwhile, a DCFS enrichment kinetic curve was much fitted by the pseudo-second-order kinetic model and DCFS enrichment isothermal curve was close to the Freundlich isothermal model, indicating the dependence of DCFS quantity enriched by TAPAM-PDA-Fe$_3$O$_4$ and a multilayer heterogeneous enrichment process. The degradation experiment confirmed that DCFS was effectively degraded by ultraviolet/H$_2$O$_2$/TAPAM-PDA-Fe$_3$O$_4$ and the maximum value of DCFS degradation efficiency reached 98.1%. Furthermore, the regeneration experiment showed that the enrichment and degradation efficiency of DCFS could maintain a relatively high level in the initial three recycles.

Keywords: diclofenac sodium; π–π stacking; charge neutralization; enrichment; degradation

1. Introduction

Diclofenac sodium (DCFS) represents a rising concern due to its ecotoxicological potential and current, sustained release into the aquatic environment. Furthermore, many regions and countries, such as Europe, America, China, and so on, have added DCFS to the priority substances monitoring list of water policy [1–3]. Approximately a hundred tons of DCFS are sold annually worldwide, about 15% of which is excreted unchanged by human race and is frequently detected in domestic wastewater [4]. In addition, the ever-increasing global population is expected to cause a sharp increase in the emissions of DCFS in the future. Several studies have shown that DCFS exposure demonstrates bioaccumulation in invertebrates, which has an ecotoxicological risk to the aquatic food chain [5]. At present, due to the

limited biodegradability of sewage treatment plants, DCFS can't be effectively dislodged by traditional sewage treatment methods [6–9].

Several technologies have been studied to reduce the DCFS concentration in aqueous environments, such as photolysis and electro-Fenton based treatments, to give some examples [10,11]. Nevertheless, the low concentration of DCFS in domestic sewage makes it hard to degrade the pharmaceutical effectively by using these methods directly [12]. It is suggested that DCFS degradation efficiency would be enhanced by realizing DCFS enrichment before degradation process. There are also several studies on the enrichment of DCFS from water, which provide the possibility to realize the combination of DCFS enrichment and degradation [13–15].

Anion polyacrylamide (APAM) synthesized by acrylamide and 2-acrylamido-2-methyl-1-propanesulfonic acid (AMPS) is a typical class of organic flocculant with high intrinsic viscosity and electronegative properties. The molecular chains of APAM could induce charge neutralization to remove cationic organics from wastewater [16].

Meanwhile, dopamine (DA), which is environment-friendly and energy-efficient, could undergo self-polymerization by ultraviolet (UV) radiation. So far polydopamine (PDA) has been applied in various areas, such as wastewater treatment, drug loading capsules and organic catalysts considering its biocompatible, good thermal stability and amazing adhesion on various materials since its first report by Messersith and his colleagues in 2007 [17–19]. It is interesting to note that polydopamine and DCFS are both rich in aromatic rings, which may lead to the π–π stacking effect between them [20].

Moreover, response surface methodology (RSM) is widely adopted in the area of parameter optimization, which includes Doehlert matrix, central composite designs, and Box-Behnken design (BBD) [21,22]. Among them, BBD is more efficient and it can be used by relatively few combinations of variables to determine the complex response function [23].

Given that, in this study, poly(acryloyloxyethyltrimethyl ammonium chloride) (PDAC) was adopted as a cationic template, and AMPS was used as the anion monomer to react with acrylamide by copolymerization under UV irradiation, so as to prepare the template anion polyacrylamide (TAPAM) with anion micro-block structure. After that, polydopamine was used to modify the TAPAM, where magnetic Fe_3O_4 nanoparticles was grafted to realize the rapid separation from the aqueous environment, and then the novel magnetic flocculant was prepared, named template anion polyacrylamide-polydopamine-Fe_3O_4 (TAPAM-PDA-Fe_3O_4) as shown in Figure 1. Moreover, RSM was employed with BBD to optimize the synthesis of TAPAM-PDA-Fe_3O_4, and the variables chosen for the design were pH, mole ratios (PDAC/AMPS, AMPS/AM, AM/DA, DA/Fe_3O_4) and irradiation time. The new magnetic flocculant was applied to the treatment of simulated wastewater containing DCFS, and then the rapid separation of flocs from water was realized by an external magnetic field. The separated mixture was re-immersed into a lower volume dilute sulfuric acid solution to increase DCFS concentration and to generate Fe^{2+} by grafted Fe_3O_4 nanoparticles. After adding the appropriate amount of H_2O_2 to the solution, it was settled in a UV irradiation environment. Finally, it was expected to realize the rapid enrichment, separation, and degradation of DCFS in order to overcome the related problems.
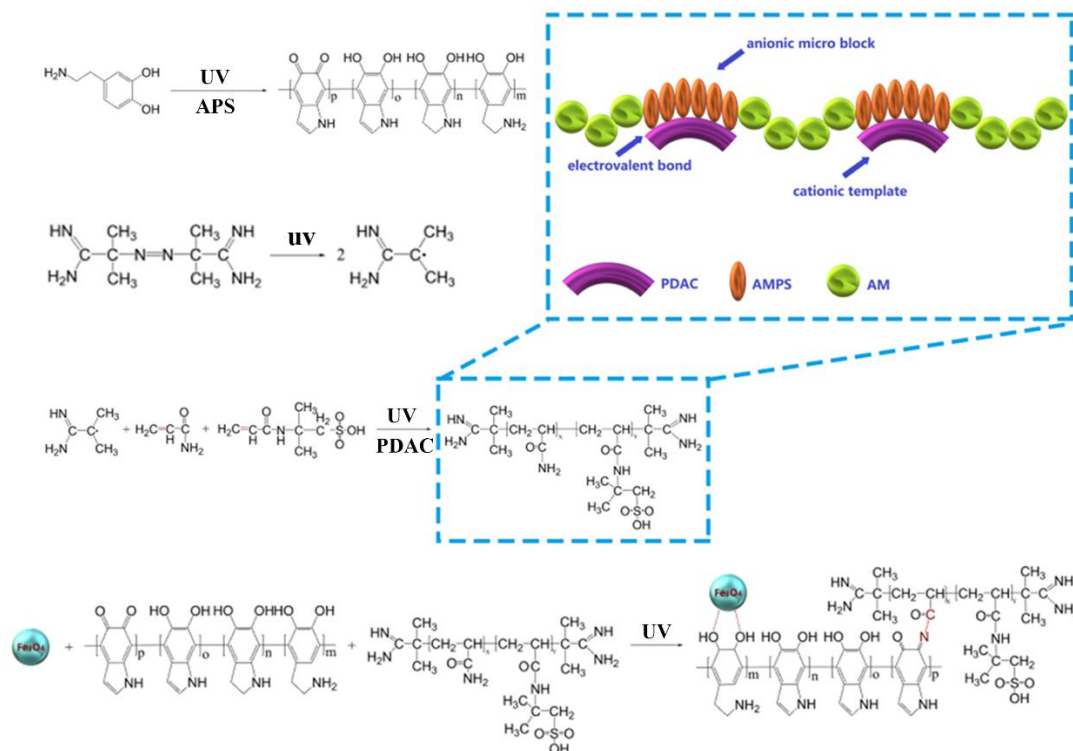
Figure 1. The scheme of preparing TAPAM-PDA-Fe$_3$O$_4$.

2. Materials and Methods

2.1. Materials

Acrylamide (AM) and acryloyloxyethyltrimethyl ammonium chloride (DAC) were purchased from Chongqing Lanjie Tap Water Company (Chongqing, China). Diclofenac sodium was obtained from Chengdu Kelong Chemical Reagent Corporation (Chengdu, China). 2-acrylamido-2-methyl-1-propanesulfonic acid (AMPS) was sourced from Shouguang Chemical Co. Ltd. (Shouguang, China). Photo-initiator 2,2′-azobis(2-methylpropionamide) dihydrochloride (V-50) was purchased from Ruihong biological technology Co. Ltd. (Shanghai, China). Dopamine hydrochloride ammonium persulfate was purchased from Aladdin Industrial Inc. (Shanghai, China). AM and AMPS were technical grade and the other reagents used in this study were analytical grade. All chemicals were used without further treatment and all solutions were prepared with ultrapure water (18 MΩ cm).

2.2. TAPAM-PDA-Fe$_3$O$_4$ Synthesis Optimization

The preparation of TAPAM-PDA-Fe$_3$O$_4$ described in Text S1 was optimized by Box-Behnken Design (BBD) and response surface method (RSM). Six factors: pH (X_1), mole ratio of PDAC/AMPS (X_2), AMPS/AM (X_3), AM/DA (X_4), DA/Fe$_3$O$_4$ (X_5) and irradiation time (X_6) were selected as the independent variables. Intrinsic viscosity was chosen as the response variable. As shown in Table 1 and Supplementary Table S1, B$_{54}$ (3^6) was used to improve the experiment and Supplementary Equation (S1) was used to predict the optimal condition.

Table 1. The independent variables levels designed in the B_{54} (3^6).

Independent Variables	Code	Levels		
		−1	0	1
pH	X_1	5	7.5	10
n_1 (PDAC: AMPS)	X_2	0.5	1.25	2
n_2 (AMPS: AM)	X_3	0.2	2.6	5
n_3 (AM: DA)	X_4	1	3.5	6
n_4 (DA: Fe_3O_4)	X_5	1	3.5	6
Irradiation time (min)	X_6	30	75	120

2.3. Analytical Methods

FT-IR spectra were measured by a spotlight 200 FT-IR spectrometer (Nicolet IS10, Thermo Fisher Scientific, Waltham, MA, USA). X-ray photoelectron spectroscopy spectra was detected by the ESCALAB250Xi XPS spectrometer (Thermo Fisher Scientific, Waltham, MA, USA). Chemical constituents and thermal stability of the products were analyzed by a DTG-60H synchronal thermal analyzer (SHIMADZU, Kyoto, Japan). The morphology and fractal dimension of magnetic flocculant were detected by the high-resolution field emission scanning electron microscope (SEM, Quattro S, Thermo Fisher Scientific, Waltham, MA, USA) coupled with Image-Pro software (plus 6.0, Media Cybernetics, Rockville, MA, USA). The magnetic properties and crystal phases of magnetic flocculant were analyzed by a vibrating sample magnetometer (PPMS DynaCool 9, Quantum Design, San Diego, CA, USA) and a X-ray diffractometer (7000, Shimadzu, Kyoto, Japan), respectively. A Nano ZS90Zetasizer (Malvern Instruments Co. Ltd, Malvern, UK) was used to analyze zeta potential of DCFS aqueous solution.

2.4. Enrichment Experiments

DCFS standard aqueous solution of 2.0 mg L^{-1} was prepared in the lab, and the corresponding predetermined concentration (0.1, 1.0, 1.5, 2.0 mg L^{-1}) was accurately prepared by diluting standard aqueous solution with ultrapure water. Standard TAPAM–PDA-Fe_3O_4 suspension of 10 mg mL^{-1} was prepared by adding 0.1 g TAPAM–PDA-Fe_3O_4 into 10 mL deionized water and then 0.5, 1.0, 1.5, 2.0, 2.5 and 3.0 mL of that were separately added into 250 mL DCFS solution of predetermined concentration. A program-controlled ZR4-6 jar test apparatus (Shenzhen Zhongrun Water Industry Technology and Development Co. Ltd, Shenzhen, China) was used to carry out enrichment experiment at ambient temperature and the mixture was stirred vigorously (300 rpm) for 1 min, then was stirred moderately (160 rpm) for 4 min, and finally stirred slowly (40 rpm) for 5 min. The rapid separation of magnetic flocculant from aqueous environment was achieved by settling a circular magnet under the beaker and the sample was extracted from 1 cm under the aqueous solution surface to detect the remained concentration by HPLC-UV (WATERS, Milford, MA, USA) combined with the COSMOSIL 3C_{18}-MS-II column (Nacalai Tesque, Inc., Kyoto, Japan) at 276-nm detection wavelength. A mixture of acetic acid solution (3.0%)/acetonitrile (80:20) was used as the mobile phase, the flow rate and the largest injection volume of which were 1.0 mL min^{-1} and 50 μL, respectively. All results of DCFS remained concentration were averaged with three averaged measurements and the scale bar was obtained by calculating the standard deviation of the three values. The removal efficiency is described by Equation (1):

$$\text{Removal efficiency} = \left(1 - \frac{C_f}{C_i}\right) \times 100\% \tag{1}$$

where C_i and C_f are for the initial and the final concentration of DCFS, respectively.

2.5. Degradation Experiments

The separated magnetic flocculant prepared in Section 2.4 was then added into the 25 mL quartz conical flask with 10 mL dilute sulfuric acid solution (0.1 M) to generate Fe^{2+} by grafted Fe_3O_4 nanoparticles, and the pH was adjusted to 4.5. The concentration of Fe^{2+} in the sample after 60 min settlement was measured by the phenanthroline-colorimetric method. Then, a predetermined amount of H_2O_2 (n (Fe^{2+}):n (H_2O_2) = 1:4) was injected into the solution. Meanwhile, the DCFS solution treated directly with Fe_3O_4/H_2O_2/sulfuric acid was used as control. The concentration of Fe^{2+}, H_2O_2 and sulfuric acid in the control group was equal to that in the experimental group. The samples were both irradiated under UV environment at 365 nm wavelength by a GY-500 high-pressure mercury lamp for 60 min. The remaining amount of DCFS before and after irradiation was also detected by HPLC-UV (WATERS, Milford, MA, USA) and the degradation efficiency was calculated by Equation (1). The degradation products of DCFS were identified by ultraperformance liquid chromatography coupled with Vion ion mobility separation quadrupole time-of-flight tandem mass spectrometry (UPLC-Vion IMS Q-TOF-MS, ACQUITY I class, Waters, Milford, MA, USA).

2.6. Stability and Regeneration of TAPAM-PDA-Fe₃O₄

Stability and regeneration experiments were carried out to investigate the potential of TAPAM-PDA-Fe_3O_4 reutilization. After enrichment and degradation of sections of DCFS, the magnetic flocculant was extracted by an external magnetic field and revised by ethanol for three times, and it was used to repeat experiments in Sections 2.4 and 2.5, and processed for five cycles. The removal and degradation efficiency of DCFS was analyzed by the method mentioned above. Thereafter, the FT-IR spectra of used TAPAM-PDA-Fe_3O_4 were obtained and virgin TAPAM-PDA-Fe_3O_4 was used as control. Meanwhile, the Fe^{2+} concentration of the solution settled for 60 min of every cycle containing sulfuric acid/TAPAM-PDA-Fe_3O_4 was detected by the method cited in Section 2.5. Further, the original DCFS solution (equal amount of DCFS) of every cycle, which contained an equal mass of Fe_3O_4 and the same concentration of sulfuric acid was used as control.

3. Results and Discussion

3.1. TAPAM-PDA-Fe₃O₄ Synthesis Optimization

The least square method shown in Supplementary Table S1 was used to measure the intrinsic viscosity regression model in consideration of the six factors. The regression model variance analysis and regression equation were presented in Supplementary Table S2 and Supplementary Equation (S2), respectively. As shown in Supplementary Table S2, the *p*-value was no more than 0.0001, suggesting statistical significance. Furthermore, X_1, X_3, X_6, X_{12}, X_{32}, and X_{62} were significant model terms. The interaction effects of X_1, X_3 and X_1, X_6 on the intrinsic viscosity of TAPAM-PDA-Fe_3O_4 were depicted in Figure 2. The intrinsic viscosity TAPAM-PDA-Fe_3O_4 increased slightly with the increase of X_3 (0.2–1.4) and then decreased as the X_3 further increased (1.4–5.0) as shown in Figure 2A. On the contrary, the intrinsic viscosity increased significantly with the increase of X_1 (5.0–8.5), then decreased slightly as the X_1 further increased (8.5–10.0). It was more significant that pH showed on intrinsic viscosity of TAPAM-PDA-Fe_3O_4 than mole ratio of AMPS/AM as depicted in Figure 2A. The intrinsic viscosity of TAPAM-PDA-Fe_3O_4 strengthened sharply with the increase of X_6 (30–75 min) and then decreased significantly as the X_6 further increased (75–120 min) as presented in Figure 2B. The other factors (X_2, X_4, X_5) had no significant effect on the intrinsic viscosity of TAPAM-PDA-Fe_3O_4 indicated from Supplementary Table S2. Furthermore, the simulated maximum value of by RSM was 1721.5 mL g^{-1} (X_1 = 8.6, X_2 = 0.50, X_3 = 1.27 X_4 = 1.48, X_5 = 3.29, and X_6 = 86.0 min). Moreover, six parallel TAPAM-PDA-Fe_3O_4 synthesis processes were carried out according to the theoretical optimal conditions. The actual intrinsic viscosity mean value was 1710.7 mL g^{-1}, which was close to the simulated value, indicating the appositeness of the theoretical optimal condition.
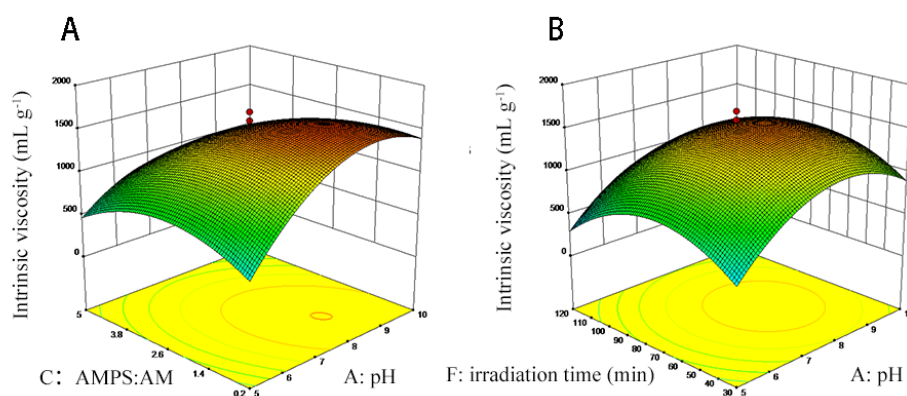
Figure 2. RSM analysis for the effect of pH coupled with mole ratio of AMPS/AM (**A**) and for the effect of pH combined with irradiation time (**B**).

3.2. Characterization of Magnetic Flocculant

### 3.2.1. FT-IR and XPS Spectral Analysis

Figure 3A illustrates the FT-IR spectra of TAPAM-PDA-Fe_3O_4, TAPAM-Fe_3O_4, and APAM-Fe_3O_4, respectively. As for TAPAM-PDA-Fe_3O_4, the characteristic peaks at 3336 cm^{-1} and 3187 cm^{-1} belong to the phenolic O–H and N–H stretching vibration, the peak at 1650 cm^{-1} was attributed to the aromatic ring stretching vibration and N–H bending vibration, the peak at 1545 cm^{-1} inclined the N–H shearing vibration, the peak at 1411 cm^{-1} was caused by phenolic C–O–H bending vibration, and the peak at 1117 cm^{-1} was due to C–O vibration, suggesting that PDA was grafted onto TAPAM successfully [24,25]. Furthermore, the peak at 1604 cm^{-1} was due to the C=O stretching vibration from AM and AMPS. Meanwhile the –SO_3H– stretching bands from AMPS was found at 1088 and 1039 cm^{-1} [26,27]. As for APAM-Fe_3O_4 and TAPAM-Fe_3O_4, it was found that the C=O peak area at 1643 cm^{-1} in TAPAM-Fe_3O_4 was larger than that at 1636 cm^{-1} in APAM-Fe_3O_4. Furthermore, the wide scan XPS spectra of the TAPAM-PDA-Fe_3O_4, TAPAM-Fe_3O_4 and APAM-Fe_3O_4 was depicted in Figure 3B for analyzing the Fe_3O_4 nanoparticles distribution on the flocculants surface. The photoelectron lines at binding energies of 709.2 eV corresponding to Fe_{2p} were both found in curves of TAPAM-Fe_3O_4 and TAPAM-PDA-Fe_3O_4, but they didn't exist in the curve of APAM-Fe_3O_4 (see dotted circles). As a result, PDAC used as the cationic template made the negative groups of AMPS more concentrated in the polymer chain and TAPAM grafted by PDA had abandon catechol groups, which may both contribute to make more Fe_3O_4 nanoparticles distribute on the flocculant surface and enhance the flocculant magnetic properties. Meanwhile, the binding energy of 166.3 eV related to S_{2P} was identified in the XPS spectra of APAM-Fe_3O_4 and TAPAM-Fe_3O_4, while that wasn't recognized in TAPAM-PDA-Fe_3O_4 (see dotted circles). It was suggested that –SO_3H– groups weren't exposed on the surface when PDA grafted onto the TAPAM, which may lead to a multilayer heterogeneous enrichment process. Furthermore, compared with the C1s spectra of TAPAM-Fe_3O_4 and APAM-Fe_3O_4, the C1s spectra of TAPAM-PDA-Fe_3O_4 was deconvoluted into five components corresponding to C=C (283.7 eV), C–C (284.1 eV), C–N (286.0 eV), C–O (287.2 eV) and C=O (288.2 eV), which was depicted in Figure S1 [28,29]. It was further confirmed that abundant aromastic rings with hydroxyl groups were grafted on TAPAM.
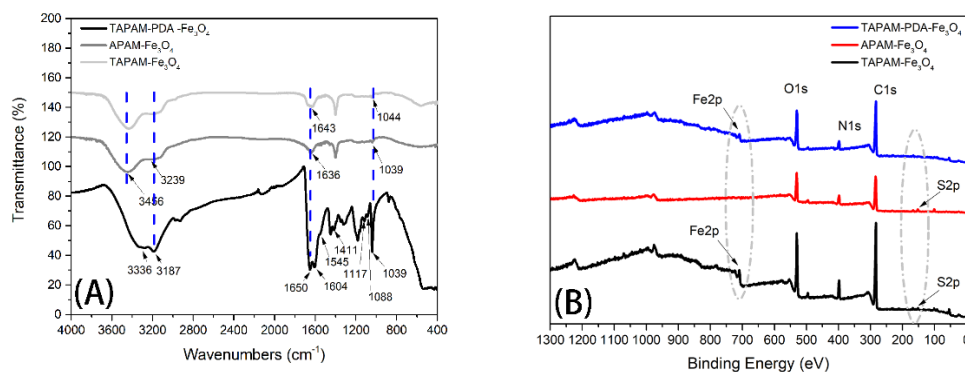
Figure 3. FT-IR (**A**) and XPS (**B**) spectra of TAPAM-PDA-Fe$_3$O$_4$, APAM-Fe$_3$O$_4$ and TAPAM-Fe$_3$O$_4$ (the dotted lines and dotted circles are corresponding to the peaks mentioned in Section 3.2.1).

3.2.2. TGA-DSC Analysis

Figure 4A–C show the Thermo Gravimetric and differential scanning calorimetry analysis (TGA-DSC) curves of APAM-Fe$_3$O$_4$, TAPAM-Fe$_3$O$_4$, and TAPAM-PDA-Fe$_3$O$_4$, respectively. It was observed in the TGA curves that four main stages for A and B and three main stages for C exist. The initial stages of the three TGA curves ranged 103.0–209.7 °C, 119.0–197.0 °C, and 164.5–229.6 °C with partial weight loss of about 5.77% for A, 3.29% for B, and 1.32% for C, owing to the confined water molecules bonded by hydrophilic groups in the molecular chains in the synthesis process, such as –SO$_3$H– [30]. Thereafter, 10.3% weight loss (209.7–296.4 °C) for A and 14.6% weight loss (197.0–305.2 °C) for B were observed in the second stage. These results correspond to the thermal decomposition of –CO–NH– groups from A and B. The weight loss of 5.87% in the interval of 229.6–313.2 °C for C was corresponding to the thermal decomposition of aromatic rings and –CO–NH– groups [31,32]. In the third stage, 13.5% weight loss for A (296.4–357.1 °C), 14.0% weight loss for B (305.2–348.3 °C), and 7.54% weight loss for C (313.2–396.6 °C) were ascribed to the thermal decomposition of the –SO$_3$H– groups [33]. As for the fourth stage of A and B, weight loss of about 26.4% and 35.7% correspond to the thermal decomposition of the copolymer backbone [34]. It was decomposed completely above 473.9 °C for A, above 485.4 °C for B, and above 608.9 °C for C. The corresponding residual weight percentage of 44.9%, 31.9% and 78.6% was corresponding to the residual Fe$_3$O$_4$ and carbon black, respectively [35]. The DSC curves of A and B both showed apparent four peaks of heat absorption appearing at 195.2 °C, 257.9 °C, 329.0 °C, 351.3 °C and at 159.9 °C, 302.8 °C, 320.5 °C, 366.7 °C, respectively. It was the derivative values of the corresponding TGA curves inflection points. Similarly, three heat absorption peaks appearing at 177.3, 284.8 and 366.3 °C for C were corresponding to the three inflection points of the TGA curve. These results demonstrated that APAM-Fe$_3$O$_4$, TAPAM-Fe$_3$O$_4$ and TAPAM-PDA-Fe$_3$O$_4$ had thermal stability between 27.9–209.7 °C, 28.1–197.0 °C and 29.4–229.6 °C, respectively.
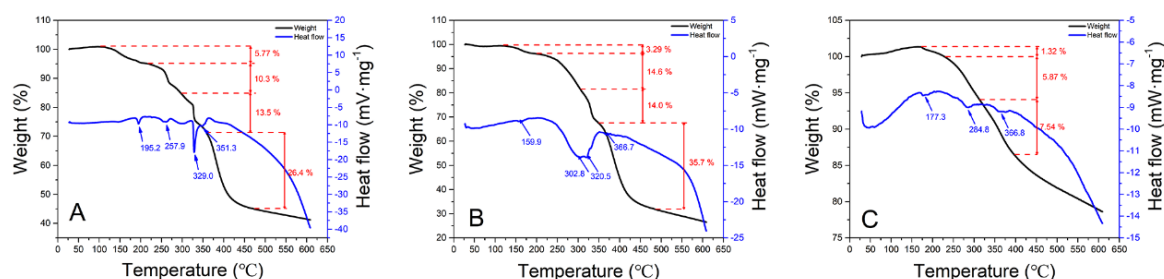

Figure 4. TGA-DSC analysis of (**A**) APAM-Fe$_3$O$_4$, (**B**) TAPAM-Fe$_3$O$_4$ and (**C**) TAPAM-PDA-Fe$_3$O$_4$.

3.2.3. Morphological Analysis

A vacuum freeze dryer was used to treat the samples to preserve the surface morphology of samples. The micro-structures of APAM-Fe$_3$O$_4$, TAPAM-Fe$_3$O$_4$ and TAPAM-PDA-Fe$_3$O$_4$ at a scale of

10 µm/500 nm were shown in Figure 5. The corresponding fractal dimensions of 1.2786, 1.3154, and 1.3639 are also shown in Figure 5, respectively. Interestingly, the specific surface area of APAM-Fe$_3$O$_4$, TAPAM-Fe$_3$O$_4$ and TAPAM-PDA-Fe$_3$O$_4$ increased gradually while the average particle size was reduced in sequence. The surfaces of the three magnetic flocculants were not smooth, which was caused by the self-assembly of polymer chains to form particles, and the particles are intertwined to form a porous network structure. It is favorable that enhancing the flocculation and bridging effect in the flocculation process. Furthermore, the morphology of APAM-Fe$_3$O$_4$, TAPAM-Fe$_3$O$_4$, and TAPAM-PDA-Fe$_3$O$_4$ changed gradually from fluffy to compact. This was caused by two reasons, on one hand, the template polymerization made the negative charge distribution more concentrated on the polymer chain so that the macromolecule backbone was more extended, which was favorable for the magnetic flocculant to form a lattice-like structure. On the other hand, the catechol groups from grafted PDA were strongly negative charged in the aqueous environment so that the internal charge repulsion of the molecular chain was increased, and the abundant aromatic rings from grafted PDA increased the inner-chain steric hindrance, which made the magnetic flocculant more spread in the aqueous environment. The lattice-like structure was further enhanced.
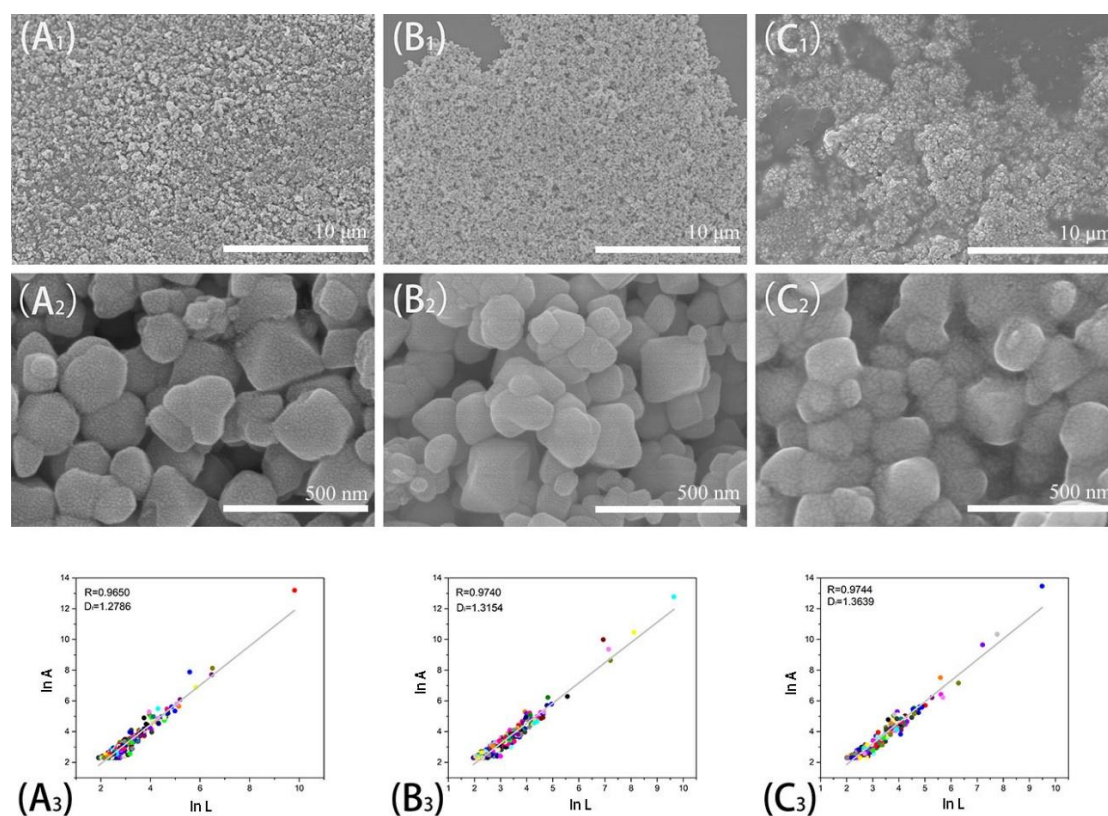

Figure 5. SEM and fractal dimensions of APAM-Fe$_3$O$_4$ (**A$_1$,A$_2$,A$_3$**), TAPAM-Fe$_3$O$_4$ (**B$_1$,B$_2$,B$_3$**) and TAPAM-PDA-Fe$_3$O$_4$ (**C$_1$,C$_2$,C$_3$**). (The dots in A$_3$, B$_3$ and C$_3$ were corresponding to the linear correlation of the logarithm of projected area A and the characteristic length L).

3.2.4. XRD Patterns

It was shown in Figure 6A that the XRD pattern curves of Fe$_3$O$_4$, TAPAM-PDA-Fe$_3$O$_4$, TAPAM-Fe$_3$O$_4$ and APAM-Fe$_3$O$_4$, respectively. The characteristic diffraction peaks of Fe$_3$O$_4$ in TAPAM-PDA-Fe$_3$O$_4$ and TAPAM-Fe$_3$O$_4$ were confirmed, indicating that the Fe$_3$O$_4$ crystal phase was unchanged after the polymerization section. However, there were not any characteristic peaks of Fe$_3$O$_4$ observed in APAM-Fe$_3$O$_4$, suggesting that the Fe$_3$O$_4$ nanoparticles were enmeshed into the polymer chain, which corresponds to the XPS analysis results. In addition, a broad peak at 22.7 °C, was observed, indicating the wrinkled surface structure of organic fraction.
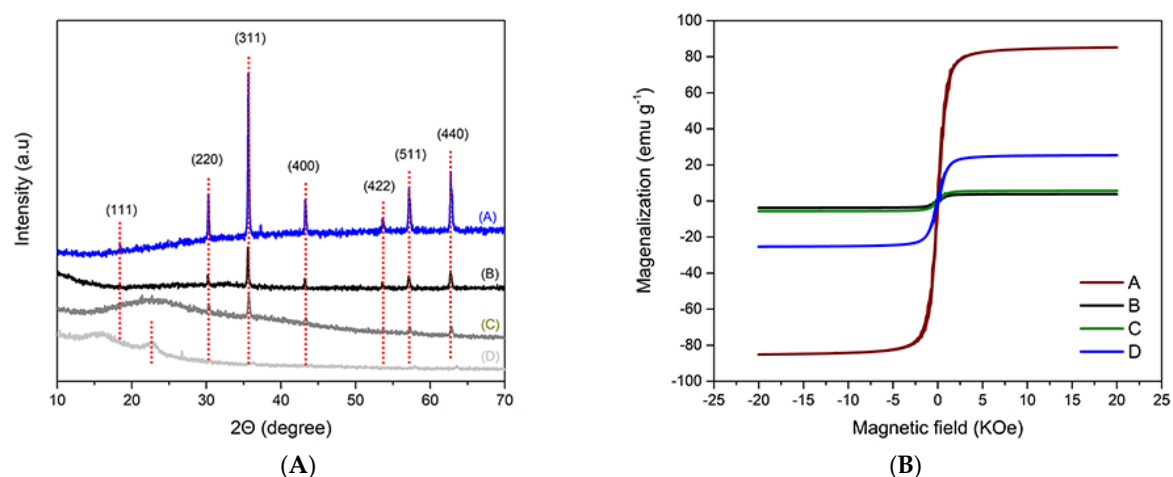
Figure 6. (**A**) XRD patterns and (**B**) magnetization curves of (A) Fe$_3$O$_4$, (B) APAM-Fe$_3$O$_4$ (C) TAPAM-Fe$_3$O$_4$ and (D) TAPAM-PDA-Fe$_3$O$_4$.

3.2.5. Magnetic Properties

As shown in Figure 6B, the saturation magnetization value was measured to be 25.3 emu g^{-1} for TAPAM-PDA-Fe$_3$O$_4$, 5.7 emu g^{-1} for TAPAM-Fe$_3$O$_4$, 3.8 emu g^{-1} for APAM-Fe$_3$O$_4$, and 85.1 emu g^{-1} for Fe$_3$O$_4$. The saturation magnetization value of TAPAM-PDA-Fe$_3$O$_4$ was relatively much higher than that of TAPAM-Fe$_3$O$_4$ or APAM-Fe$_3$O$_4$. It suggested that Fe$_3$O$_4$ nanoparticles chelated with grafted PDA was contributed to enhance the magnetization of flocculant. Although the saturation magnetization of TAPAM-PDA-Fe$_3$O$_4$ decreased compared with Fe$_3$O$_4$ particles, it could significantly facilitate the separation of flocs by an external magnetic field.

3.3. Enrichment Properties

3.3.1. DCFS Initial Concentration Effect

The enrichment capability of TAPAM-PDA-Fe$_3$O$_4$ for removing various concentration DCFS was investigated and APAM-Fe$_3$O$_4$ and TAPAM-Fe$_3$O$_4$ were used as control. For all three kinds of magnetic flocculants, the removal efficiency was higher as the DCFS initial concentration was 0.1 mg L^{-1} instead of 1.0, 1.5 and 2.0 mg L^{-1}, as shown in Figure 7A–C. It was because that steric hindrance between DCFS and polymer chain was enhanced when DCFS initial concentration exceeded a certain value, which negatively affected the removal efficiency. It was also found that TAPAM-PDA-Fe$_3$O$_4$ had better DCFS removal efficiency than APAM-Fe$_3$O$_4$ or TAPAM-Fe$_3$O$_4$. The maximum removal efficiency of APAM-Fe$_3$O$_4$, TAPAM-Fe$_3$O$_4$ and TAPAM-PDA-Fe$_3$O$_4$ was 49.1%, 66.2%, and 99.1% as the DCFS concentration was 0.1 mg L^{-1}, respectively. This phenomenon could be explained as follows. On one hand, the anion block structure made the negative charge more concentrated and strengthened the charge neutralization effect. On the other hand, the TAPAM modified by PDA had abandoned aromatic rings and absorbed DCFS through π–π stacking effect, which further improved the DCFS removal efficiency. As a result, the 0.1 mg L^{-1} DCFS was used in the following sections.
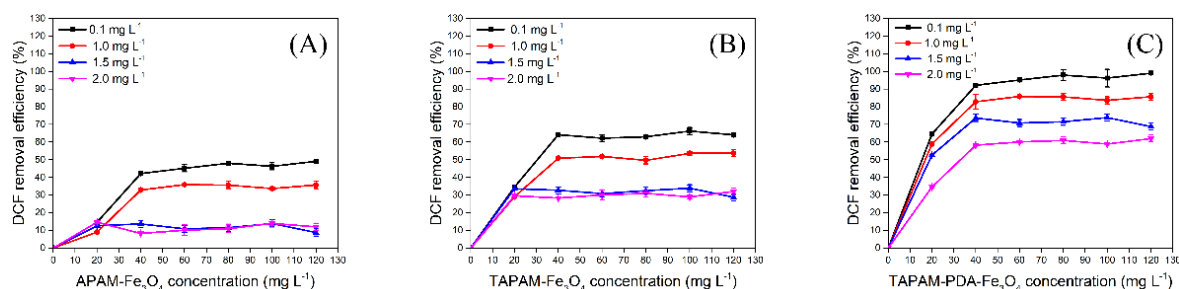
Figure 7. Effect of the DCFS initial concentration on enrichment properties ((**A**) for APAM-Fe$_3$O$_4$, (**B**) for TAPAM-Fe$_3$O$_4$, (**C**) for TAPAM-PDA-Fe$_3$O$_4$).

3.3.2. DCFS Initial pH Effect

The enrichment performance of APAM-Fe$_3$O$_4$, TAPAM-Fe$_3$O$_4$, and TAPAM-PDA-Fe$_3$O$_4$ was investigated under the conditions of various DCFS initial pH values. As seen in Figure 8A, in the range of pH 1.0–3.0, the DCFS removal efficiency was increased when the sample was treated by APAM-Fe$_3$O$_4$. In the interval of pH 3.0–8.0, the DCFS removal efficiency was maintained between 68.2%–72.4%. However, it decreased dramatically to 3.0% when the initial pH further increased to 12.0. As for TAPAM-Fe$_3$O$_4$ and TAPAM-PDA-Fe$_3$O$_4$, the removal efficiency curves of DCFS had the similar trend. In the range of pH 4.0–9.0, the enrichment performance of TAPAM-Fe$_3$O$_4$ and TAPAM-PDA-Fe$_3$O$_4$ was both better than that of APAM-Fe$_3$O$_4$. Furthermore, the enrichment performance of TAPAM-PDA-Fe$_3$O$_4$ was much better in the interval of pH 5.0–9.0, and DCFS removal efficiency was above 90.0% and the maximum value was above 95.0%. As a result, pH 8.0 was used in DCFS enrichment kinetics and isotherms analysis.
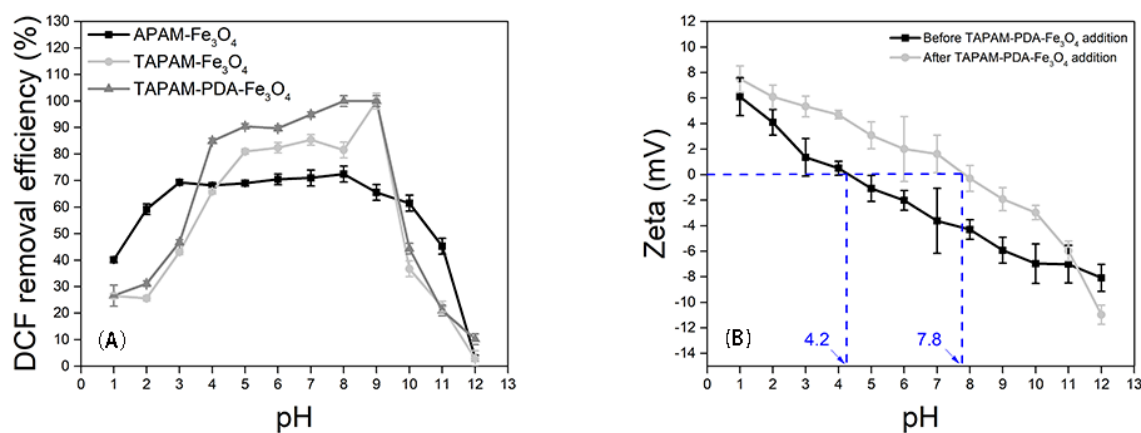

Figure 8. DCFS initial pH effect on the enrichment performance (**A**) and DCFS zeta potential at different pH before and after TAPAM-PDA-Fe$_3$O$_4$ injection (**B**).

3.3.3. Enrichment Mechanism Analysis

The enrichment mechanism of TAPAM-PDA-Fe$_3$O$_4$ was further investigated. It was illustrated in Figure 8B that DCFS zeta potential obtained both before and after TAPAM-PDA-Fe$_3$O$_4$ treatment at different pH value. The DCFS isoelectric point was located at pH 4.2 before TAPAM-PDA-Fe$_3$O$_4$ treatment. However, the DCFS isoelectric point was around pH 7.8 after TAPAM-PDA-Fe$_3$O$_4$ addition, which was ascribed to the charge neutralization between –NH$^+$ groups in DCFS and –SO$_3$H– groups in TAPAM-PDA-Fe$_3$O$_4$. Furthermore, high DCFS maximum removal efficiency at pH 9.0 known from Figure 8A indicated the involvement of π–π stacking between DCFS and TAPAM-PDA-Fe$_3$O$_4$. At pH 10.0, the maximum removal efficiency reached 44.3%, which indicates that under relatively strong alkaline conditions, the electrostatic repulsion between the negatively charged groups also leads to a decrease in the π–π stacking efficiency, and the enmeshment/sweeping effect played a considerable

role. In a nutshell, the whole process is depicted in Figure 9. First, DCFS was absorbed by abundant aromatic rings in TAPAM-PDA-Fe$_3$O$_4$ through π–π stacking in the interval of 7.0 < pH < 9.0. Second, it was charge neutralization between DCFS and –SO$_3$H– groups in TAPAM-PDA-Fe$_3$O$_4$ that worked in the range of 1.0 < pH < 4.2. At last, large flocs were formed by the aggregation of small flocs through the external magnetic field.
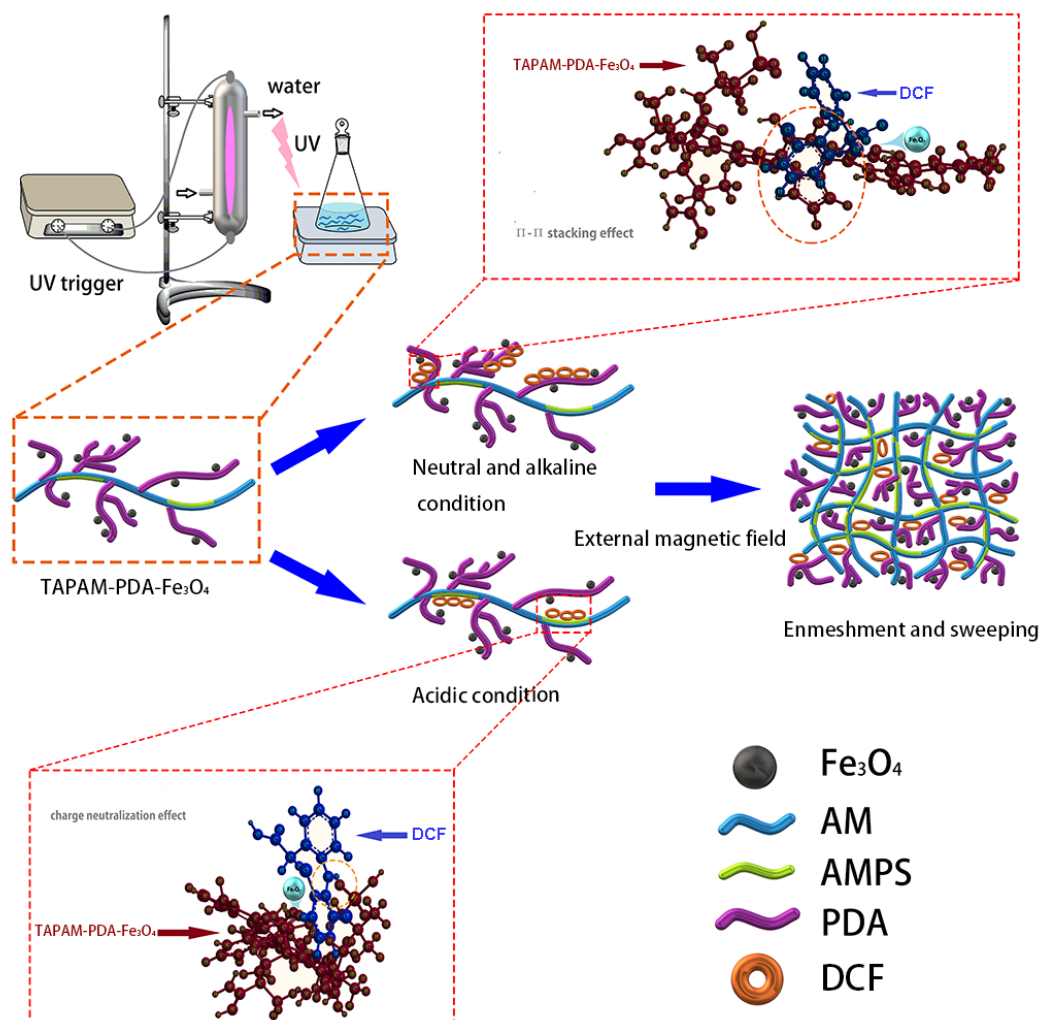
Figure 9. The scheme of DCFS enrichment mechanism by TAPAM-PDA-Fe$_3$O$_4$. (The detail schemes of the TAPAM-PDA-Fe$_3$O$_4$ structure, π–π stacking and charge neutralization effect were depicted in the dotted circles.)
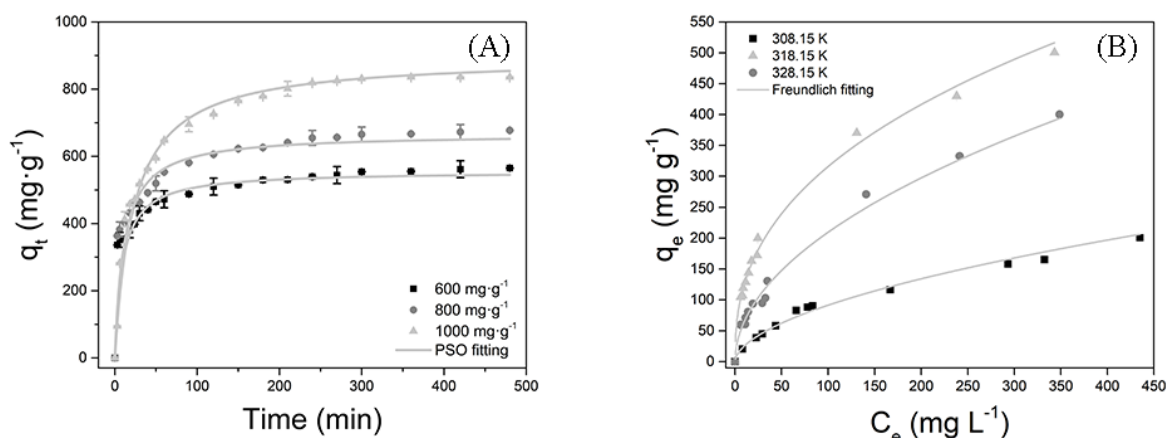
3.3.4. DCFS Enrichment Kinetics Analysis

The DCFS enrichment kinetics treated by TAPAM-PDA-Fe$_3$O$_4$ were investigated by pseudo-first order (PFO), pseudo-second order (PSO), and intraparticle diffusion models, which were expressed as Supplementary Equation (S3)–(S5). All the obtained data were simulated by the three kinetic models. As a result, the simulated parameters were depicted in Table 2. Compared with other two models, the PSO model correlation coefficients were much closer to 1.0, meanwhile the *q* value calculated by PSO model is much closer to the actual value. This confirmed that DCFS removal rate was dependent on the quantity of DCFS flocculated onto the surface of TAPAM-PDA-Fe$_3$O$_4$ [36,37]. The PSO model simulated curves of DCFS enrichment kinetics by TAPAM-PDA-Fe$_3$O$_4$ are presented in Figure 10A. The DCFS removal rate increased sharply in the first 30 min, but slowed down thereafter. The foremost DCFS rapid enrichment was due to the accessibility of aromatic rings and –SO$_3$H– groups in TAPAM-PDA-Fe$_3$O$_4$. The succedent DCFS slow enrichment was due to the saturation of the flocculation sites.

Table 2. DCFS enrichment kinetic parameters at 318.15 K (initial pH 8.0).

Initial Concentration (mg L^{-1})	Pseudo First-Order Kinetic Model				Pseudo Second-Order Kinetic Model			Intraparticle Diffusion Kinetic Model		
	$q_{max,exp}$ (mg g^{-1})	q_e (mg g^{-1})	$k_1 \times 10^2$ (g mg^{-1} min^{-1})	R^2	q_e (mg g^{-1})	$k_2 \times 10^4$ (g mg^{-1} min^{-1})	R^2	C (mg g^{-1})	k_p	R^2
600	561.7	197.5	0.91	0.9799	555.5	1.929	0.9991	351.9	11.57	0.8949
800	672.5	272.5	0.98	0.9887	666.6	1.364	0.9989	382.8	16.22	0.9021
1000	836.1	721.8	1.82	0.9426	909.1	0.5874	0.9986	317.4	30.04	0.8052

Where q_e and $q_{max,exp}$ are the enrichment capacity of the magnetic flocculant at equilibrium and the actual maximum enrichment capacity of the magnetic flocculant, respectively. k_1 and k_2 are the rate constant of first-order and second-order flocculation, respectively. k_p is the intraparticle diffusion rate constant and R^2 is the correlation coefficient.

Figure 10. Enrichment kinetics of DCFS (**A**) and enrichment isotherms of DCFS (**B**) by TAPAM-PDA-Fe$_3$O$_4$ treatment.

3.3.5. DCFS Enrichment Isotherms Analysis

The obtained experimental data were simulated by Dubinin-Radushkevich, Freundlich, and Langmuir isotherm models, which were expressed as Supplementary Equation (S6)–(S8). The final fitted parameters are all depicted in Table 3. It was conformed that Freundlich model correlation coefficients were much close to 1.0, suggesting that a multilayer heterogeneous flocculation of DCFS occurred onto the TAPAM-PDA-Fe$_3$O$_4$ [38,39]. In addition, the Freundlich isotherm simulated curves of DCFS at different temperatures were depicted in Figure 10B. The DCFS enrichment efficiency at 318.15 K was better than that at 308.15 K or 328.15 K. This indicated that the Brownian motion principle between DCFS and TAPAM-PDA-Fe$_3$O$_4$ had a great influence on the enrichment process. To some extent, it increased the collision possibility between DCFS and TAPAM-PDA-Fe$_3$O$_4$, which was positively contributed to DCFS enrichment. While beyond a certain limit, confined DCFS molecules by TAPAM-PDA-Fe$_3$O$_4$ tended to escape, which weakened DCFS enrichment process.

Table 3. Isotherm parameters for DCFS enrichment treated by TAPAM-PDA-Fe$_3$O$_4$ at pH 8.0.

T (K)	Langmuir Isotherm Model				Freundlich Isotherm Model			D-R Isotherm Model		
	k_L (L mg^{-1})	q_{max} (mg g^{-1})	R_L [a]	R^2	k_F	n	R^2	q_d (mg g^{-1})	$k_d \times 10^6$ (mol^2 kJ^{-2})	R^2
298.15	0.02	144.9	0.048	0.965	7.15	1.81	0.994	124.7	1.74	0.748
308.15	0.044	366.3	0.022	0.946	50.4	2.51	0.997	361.6	1.22	0.862
318.15	0.025	266	0.038	0.935	20.5	1.98	0.998	261.8	1.9	0.806

k_L is for the Langmuir isotherm constant, k_F is corresponding to the Freundlich isotherm constant, k_d is the constant related to the mean free energy of flocculation and R_L [a] is the separation factor related to Langmuir model.

3.4. Degradation Performance

As shown in Figure 11A, the total amount of DCFS in the two samples separately was equal (25 μg) and when the DCFS simulated wastewater (0.1 mg L^{-1}) was directly treated with UV/H$_2$O$_2$/Fe$_3$O$_4$, the degradation efficiency was low because of the low DCFS concentration. Meanwhile, the maximum degradation efficiency was 31.1% and the residual amount of DCFS was 17.2 μg after 30 min UV irradiation. However, the maximum degradation efficiency reached 98.1% and the DCFS residual amount was 0.48 μg when it was under UV/H$_2$O$_2$/TAPAM-PDA-Fe$_3$O$_4$ enrichment-degradation (E-D) treatment. This suggested that DCFS degradation could be realized efficiently when the enriched DCFS was re-dissolved into the dilute sulfuric acid solution (pH = 4.5) which was 0.04 times the original wastewater volume. Meanwhile, the degradation products of DCFS were identified by UPLC-Vion IMS QTOF-MS. Among the products, bis (6-methylheptyl) phthalate and 2, 6-dichloeoaniline were identified, except diclofenac sodium, which was depicted in Supplementary Figure S2. However, the degradation pathways of diclofenac sodium need further identification, and will be investigated in our next study. Moreover, various degradation processes of diclofenac sodium were summarized and compared in Table 4. It can be seen that the UV/H$_2$O$_2$/TAPAM-PDA-Fe$_3$O$_4$ process is a promising method to treat low concentration diclofenac sodium solution.
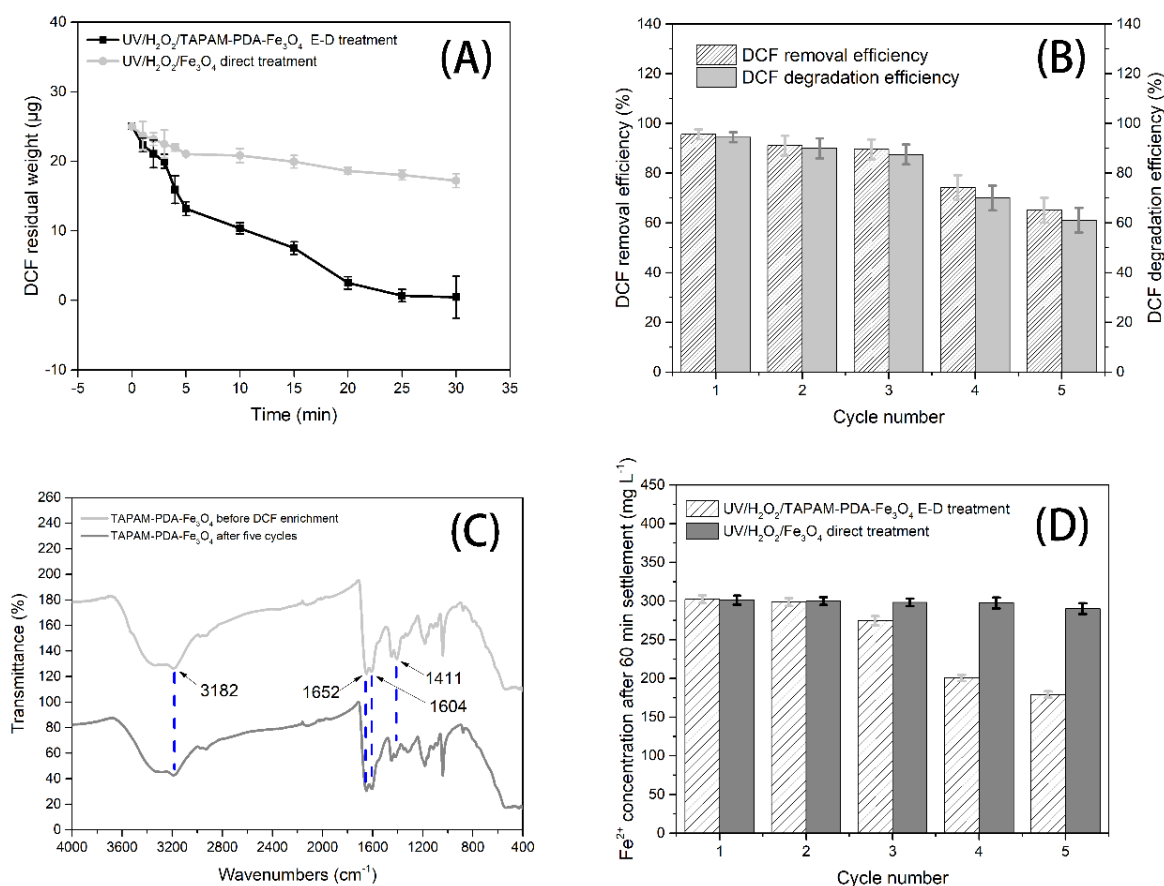
Figure 11. DCFS residual weight in the initial cycle (**A**), DCFS removal and degradation efficiency (**B**), FT-IR spectra of virgin and used TAPAM-PDA-Fe$_3$O$_4$ (**C**) and the concentration of Fe^{2+} in solution (**D**).

Table 4. Comparison of the diclofenac sodium degradation by different processes.

Processes	Water Matrix	Initial Concentration (mg L^{-1})	Degradation Conditions	Degradation Efficiency (%)	References
Photocatalysis	Aqueous solution	10	S-TiO$_2$: 0.2–0.8 g L^{-1} pH: 6.0–11.0	93.0	[40]
Photocatalysis	Aqueous solution	5	TiO2: 4 g L^{-1}	95.0	[41]
Photoelectrocatalysis	Aqueous solution	10	Persulate: 1–10 mM pH: 5.6–10.0	86.3	[42]
Photoelectrocatalysis	Aqueous solution	5	Pd/TNTs	67.7	[43]
Sonolysis	Aqueous solution	50–100	Ultrasonic frequency: 216–850 kHz	>90.0	[44]
UV/H$_2$O$_2$/TAPAM-PDA-Fe$_3$O$_4$	Aqueous solution	0.1	TAPAM-PDA-Fe$_3$O$_4$: 120 mg L^{-1} pH: 4.5	>90.0	This study

3.5. Stability and Regeneration of TAPAM-PDA-Fe$_3$O$_4$

In consideration of the stability of TAPAM-PDA-Fe$_3$O$_4$, it was reused for five cycles to enrich and degrade DCFS, and the FT-IR spectra of the revised magnetic flocculant are shown in Figure 11C. Compared with the initial TAPAM-PDA-Fe$_3$O$_4$, the characteristic peaks could be all found at 3182, 1652, and 1604 cm^{-1} in the revised magnetic flocculant. While the intensity of the characteristic peak at 1411 cm^{-1}, which is ascribed to the phenolic C–O–H bending vibration, was weaker than the virgin TAPAM-PDA-Fe$_3$O$_4$ curve. This was due to the irreversible self-assembly of TAPAM-PDA-Fe$_3$O$_4$ and parts of the catechol groups were enmeshed inside the magnetic flocculant. However, the functional groups of TAPAM-PDA-Fe$_3$O$_4$ remained relatively stable. Meanwhile, the DCFS removal efficiency and DCFS degradation efficiency both remained in the relatively high value in the initial three circles, which were separately above 90.0% and 87.0%, as shown in Figure 11B. However, the removal and degradation efficiency in the fourth and fifth cycles degraded sharply, and the corresponding minimum values were 65.1% and 59.5%, respectively. The phenomena could be explained as follows. The decrease of DCFS removal efficiency was owing to the irreversible enmeshment of TAPAM-PDA-Fe$_3$O$_4$, which led to the decreasing amount of the active function groups on the surface of the magnetic flocculant. Furthermore, the decrease of DCFS degradation efficiency was caused by two aspects. On one hand, the decrease of DCFS removal efficiency would negatively affect the concentration of the concentrated DCFS solution. On the other hand, the amount of Fe$_3$O$_4$ nanoparticles grafted on the surface of TAPAM-PDA-Fe$_3$O$_4$ decreased through reacting with sulfuric acid, which led to the sequence decrease of Fe^{2+} concentration of DCFS solution in the fourth and fifth degradation cycles, as shown in Figure 11D. However, there was little effect on the initial three removal and degradation efficiency cycles.

4. Conclusions

In this study, TAPAM-PDA-Fe$_3$O$_4$ was successfully prepared to achieve a high-level enrichment of DCFS, up to 99.1%. Furthermore, the rapid separation of flocs from aqueous environment was realized by external magnetic field and higher maximum removal efficiency could be achieved with TAPAM-PDA-Fe$_3$O$_4$ (99.1%) instead of APAM-Fe$_3$O$_4$ (49.0%) or TAPAM-Fe$_3$O$_4$ (66.2%). In neutral/alkaline condition, it was π–π stacking that had a significant impact on flocculation performance. However, in acidic conditions, charge neutralization played a leading role. In the degradation section, it was found that the degradation efficiency of DCFS by UV/H$_2$O$_2$/TAPAM-PDA-Fe$_3$O$_4$ E–D treatment could reach 98.2%, compared with which was 31.1% of UV/H$_2$O$_2$/Fe$_3$O$_4$ direct treatment. Meanwhile, the TAPAM-PDA-Fe$_3$O$_4$ could be reused effectively for three circles to realize effective enrichment and degradation of DCFS. In summary, we have designed an integrated DCFS removal system, which can reach above 90.0% removal efficiency and above 87.5% degradation efficiency in the first three cycles. Looking forward, it is possible for the UV/H$_2$O$_2$/TAPAM-PDA-Fe$_3$O$_4$ system to treat wastewater

containing DCFS effectively in relatively loose external conditions, thus holding great promise for further use in actual sewage treatment.

Supplementary Materials: The following are available online at http://www.mdpi.com/2073-4360/12/1/72/s1. Text S1: Preparation of coagulant; Table S1: Six factors Box-Behnken design and the value of response function; Table S2: Variance analysis of regression model; Figure S1: C1s XPS spectra peak fitting of TAPAM-PDA-Fe$_3$O$_4$ (A), APAM-Fe$_3$O$_4$ (B) and TAPAM-Fe$_3$O$_4$ (C); Figure S2: The products ion spectra by UPLC-Vion IMS QTOF-MS.

References

1. Fontes, M.K.; Gusso-Choueri, P.K.; Maranho, L.A.; Abessa, D.M.S.; Mazur, W.A.; de Campos, B.G.; Guimaraes, L.L.; de Toledo, M.S.; Lebre, D.; Marques, J.R.; et al. A tiered approach to assess effects of diclofenac sodium on the brown mussel Perna perna: A contribution to characterize the hazard. *Water Res.* **2018**, *132*, 361–370. [CrossRef] [PubMed]

2. Villar-Navarro, E.; Baena-Nogueras, R.M.; Paniw, M.; Perales, J.A.; Lara-Martin, P.A. Removal of pharmaceuticals in urban wastewater: High rate algae pond (HRAP) based technologies as an alternative to activated sludge based processes. *Water Res.* **2018**, *139*, 19–29. [CrossRef] [PubMed]

3. Banaschik, R.; Jablonowski, H.; Bednarski, P.J.; Kolb, J.F. Degradation and intermediates of diclofenac sodium as instructive example for decomposition of recalcitrant pharmaceuticals by hydroxyl radicals generated with pulsed corona plasma in water. *J. Hazard. Mater.* **2018**, *342*, 651–660. [CrossRef] [PubMed]

4. Rizzo, L.; Meric, S.; Kassinos, D.; Guida, M.; Russo, F.; Belgiorno, V. Degradation of diclofenac sodium by TiO$_2$ photocatalysis: UV absorbance kinetics and process evaluation through a set of toxicity bioassays. *Water Res.* **2009**, *43*, 979–988. [CrossRef] [PubMed]

5. Landry, K.A.; Sun, P.; Huang, C.H.; Boyer, T.H. Ion-exchange selectivity of diclofenac sodium, ibuprofen, ketoprofen, and naproxen in ureolyzed human urine. *Water Res.* **2015**, *68*, 510–521. [CrossRef] [PubMed]

6. Yu, H.; Nie, E.; Xu, J.; Yan, S.; Cooper, W.J.; Song, W. Degradation of diclofenac sodium by advanced oxidation and reduction processes: Kinetic studies, degradation pathways and toxicity assessments. *Water Res.* **2013**, *47*, 1909–1918. [CrossRef]

7. Forrez, I.; Carballa, M.; Verbeken, K.; Vanhaecke, L.; Ternes, T.; Boon, N.; Verstraete, W. Diclofenac sodium oxidation by biogenic manganese oxides. *Environ. Sci. Technol.* **2010**, *44*, 3449–3454. [CrossRef]

8. Xiong, T.; Yuan, X.; Wang, H.; Wu, Z.; Jiang, L.; Leng, L.; Xi, K.; Cao, X.; Zeng, G. Highly efficient removal of diclofenac sodium sodium from medical wastewater by Mg/Al layered double hydroxide-poly(m-phenylenediamine) composite. *Chem. Eng. J.* **2019**, *366*, 83–91. [CrossRef]

9. Monteagudo, J.M.; El-Taliawy, H.; Duran, A.; Caro, G.; Bester, K. Sono-activated persulfate oxidation of diclofenac sodium: Degradation, kinetics, pathway and contribution of the different radicals involved. *J. Hazard. Mater.* **2018**, *357*, 457–465. [CrossRef]

10. Avetta, P.; Fabbri, D.; Minella, M.; Brigante, M.; Maurino, V.; Minero, C.; Pazzi, M.; Vione, D. Assessing the phototransformation of diclofenac sodium, clofibric acid and naproxen in surface waters: Model predictions and comparison with field data. *Water Res.* **2016**, *105*, 383–394. [CrossRef]

11. Plakas, K.V.; Sklari, S.D.; Yiankakis, D.A.; Sideropoulos, G.T.; Zaspalis, V.T.; Karabelas, A.J. Removal of organic micropollutants from drinking water by a novel electro-Fenton filter: Pilot-scale studies. *Water Res.* **2016**, *91*, 183–194. [CrossRef]

12. De Corte, S.; Sabbe, T.; Hennebel, T.; Vanhaecke, L.; De Gusseme, B.; Verstraete, W.; Boon, N. Doping of biogenic Pd catalysts with Au enables dechlorination of diclofenac sodium at environmental conditions. *Water Res.* **2012**, *46*, 2718–2726. [CrossRef] [PubMed]

13. Wei, H.; Deng, S.; Huang, Q.; Nie, Y.; Wang, B.; Huang, J.; Yu, G. Regenerable granular carbon nanotubes/alumina hybrid adsorbents for diclofenac sodium sodium and carbamazepine removal from aqueous solution. *Water Res.* **2013**, *47*, 4139–4147. [CrossRef] [PubMed]

14. Hu, D.; Huang, H.; Jiang, R.; Wang, N.; Xu, H.; Wang, Y.G.; Ouyang, X.K. Adsorption of diclofenac sodium sodium on bilayer amino-functionalized cellulose nanocrystals/chitosan composite. *J. Hazard. Mater.* **2019**, *369*, 483–493. [CrossRef] [PubMed]

15. Espina de Franco, M.A.; de Carvalho, C.B.; Bonetto, M.M.; Soares, R.d.P.; Feris, L.A. Diclofenac sodium removal from water by adsorption using activated carbon in batch mode and fixed-bed column: Isotherms, thermodynamic study and breakthrough curves modeling. *J. Clean. Prod.* **2018**, *181*, 145–154. [CrossRef]

16. Sun, Q.; Zheng, H.; Zheng, X.; Hu, X.; An, Y.; Liu, H.; Zhao, C. Dual Polydopamine-Anion Polyacrylamide Polymer System for Improved Removal of Nickel Ions and Methylene Blue from Aqueous Solution. *Sci. Adv. Mater.* **2019**, *11*, 116–127. [CrossRef]

17. Jiang, W.; Zhang, X.; Luan, Y.; Wang, R.; Liu, H.; Li, D.; Hu, L. Using gamma-Ray Polymerization-Induced Assemblies to Synthesize Polydopamine Nanocapsules. *Polymers* **2019**, *11*, 1754. [CrossRef] [PubMed]

18. Zhao, D.; Kim, J.F.; Ignacz, G.; Pogany, P.; Lee, Y.M.; Szekely, G. Bio-Inspired Robust Membranes Nanoengineered from Interpenetrating Polymer Networks of Polybenzimidazole/Polydopamine. *ACS Nano* **2019**, *13*, 125–133. [CrossRef]

19. Ryu, J.H.; Messersmith, P.B.; Lee, H. Polydopamine Surface Chemistry: A Decade of Discovery. *ACS Appl. Mater. Interfaces* **2018**, *10*, 7523–7540. [CrossRef]

20. Chen, F.; Xing, Y.; Wang, Z.; Zheng, X.; Zhang, J.; Cai, K. Nanoscale Polydopamine (PDA) Meets pi-pi Interactions: An Interface-Directed Coassembly Approach for Mesoporous Nanoparticles. *Langmuir* **2016**, *32*, 12119–12128. [CrossRef]

21. Iregui, A.; Irusta, L.; Martin, L.; Gonzalez, A. Analysis of the Process Parameters for Obtaining a Stable Electrospun Process in Different Composition Epoxy/Poly epsilon-Caprolactone Blends with Shape Memory Properties. *Polymers* **2019**, *11*, 475. [CrossRef] [PubMed]

22. Szekely, G.; Henriques, B.; Gil, M.; Alvarez, C. Experimental design for the optimization and robustness testing of a liquid chromatography tandem mass spectrometry method for the trace analysis of the potentially genotoxic 1,3-diisopropylurea. *Drug Test. Anal.* **2014**, *6*, 898–908. [CrossRef] [PubMed]

23. Kapur, M.; Gupta, R.; Mondal, M.K. Parametric Optimization of Cu (II) and Ni (II) Adsorption onto Coal Dust and Magnetized Sawdust Using Box-Behnken Design of Experiments. *Environ. Prog. Sustain. Energy* **2016**, *35*, 1597–1604. [CrossRef]

24. Zheng, X.; Zhang, J.; Wang, J.; Qi, X.; Rosenholm, J.M.; Cai, K. Polydopamine Coatings in Confined Nanopore Space: Toward Improved Retention and Release of Hydrophilic Cargo. *J. Phys. Chem. C* **2015**, *119*, 24512–24521. [CrossRef]

25. Veisi, H.; Safarimehr, P.; Hemmati, S. Oxo-vanadium immobilized on polydopamine coated-magnetic nanoparticles (Fe_3O_4): A heterogeneous nanocatalyst for selective oxidation of sulfides and benzylic alcohols with H_2O_2. *J. Taiwan Inst. Chem. Eng.* **2018**, *88*, 8–17. [CrossRef]

26. Zheng, H.; Ma, J.; Zhu, C.; Zhang, Z.; Liu, L.; Sun, Y.; Tang, X. Synthesis of anion polyacrylamide under UV initiation and its application in removing dioctyl phthalate from water through flocculation process. *Sep. Purif. Technol.* **2014**, *123*, 35–44. [CrossRef]

27. Qiao, J.L.; Hamaya, T.; Okada, T. Chemically modified poly(vinyl alcohol)-poly(2-acrylamido-2-methyl-1-propanesulfonic acid) as a novel proton-conducting fuel cell membrane. *Chem. Mater.* **2005**, *17*, 2413–2421. [CrossRef]

28. An, Y.; Zheng, H.; Sun, Q.; Zheng, X.; Wu, Q.; Zhao, R. A novel floating adsorbents system of acid orange 7 removal: Polymer grafting effect. *Sep. Purif. Technol.* **2019**, *227*, 115677. [CrossRef]

29. Wang, J.; Chen, Z.; Chen, B. Adsorption of Polycyclic Aromatic Hydrocarbons by Graphene and Graphene Oxide Nanosheets. *Environ. Sci. Technol.* **2014**, *48*, 4817–4825. [CrossRef]

30. Yang, Z.L.; Gao, B.Y.; Li, C.X.; Yue, Q.Y.; Liu, B. Synthesis and characterization of hydrophobically associating cationic polyacrylamide. *Chem. Eng. J.* **2010**, *161*, 27–33. [CrossRef]

31. Zhao, C.; Zheng, H.; Feng, L.; Wang, Y.; Liu, Y.; Liu, B.; Djibrine, B.Z. Improvement of Sludge Dewaterability by Ultrasound-Initiated Cationic Polyacrylamide with Microblock Structure: The Role of Surface-Active Monomers. *Materials* **2017**, *10*, 282. [CrossRef] [PubMed]

32. Xing, Y.X.; Zhang, J.X.; Chen, F.; Liu, J.J.; Cai, K.Y. Mesoporous polydopamine nanoparticles with co-delivery function for overcoming multidrug resistance via synergistic chemo-photothermal therapy. *Nanoscale* **2017**, *9*, 8781–8790. [CrossRef] [PubMed]

33. Feng, L.; Zheng, H.L.; Gao, B.Y.; Zhang, S.X.; Zhao, C.L.; Zhou, Y.H.; Xu, B.C. Fabricating an anionic polyacrylamide (APAM) with an anionic block structure for high turbidity water separation and purification. *RSC Adv.* **2017**, *7*, 28918–28930. [CrossRef]

34. Liu, B.Z.; Zheng, H.L.; Deng, X.R.; Xu, B.C.; Sun, Y.J.; Liu, Y.Z.; Liang, J.J. Formation of cationic hydrophobic micro-blocks in P(AM-DMC) by template assembly: Characterization and application in sludge dewatering. *RSC Adv.* **2017**, *7*, 6114–6122. [CrossRef]

35. Zheng, C.F.; Zheng, H.L.; Wang, Y.J.; Sun, Y.J.; An, Y.Y.; Liu, H.X.; Liu, S. Modified magnetic chitosan microparticles as novel superior adsorbents with huge "force field" for capturing food dyes. *J. Hazard. Mater.* **2019**, *367*, 492–503. [CrossRef]

36. Saber-Samandari, S.; Saber-Samandari, S.; Joneidi-Yekta, H.; Mohseni, M. Adsorption of anionic and cationic dyes from aqueous solution using gelatin-based magnetic nanocomposite beads comprising carboxylic acid functionalized carbon nanotube. *Chem. Eng. J.* **2017**, *308*, 1133–1144. [CrossRef]

37. Xu, B.C.; Zheng, C.F.; Zheng, H.L.; Wang, Y.L.; Zhao, C.; Zhao, C.L.; Zhang, S.X. Polymer-grafted magnetic microspheres for enhanced removal of methylene blue from aqueous solutions. *RSC Adv.* **2017**, *7*, 47029–47037. [CrossRef]

38. Kyzas, G.Z.; Bikiaris, D.N.; Seredych, M.; Bandosz, T.J.; Deliyanni, E.A. Removal of dorzolamide from biomedical wastewaters with adsorption onto graphite oxide/poly(acrylic acid) grafted chitosan nanocomposite. *Bioresour. Technol.* **2014**, *152*, 399–406. [CrossRef]

39. Cao, J.S.; Lin, J.X.; Fang, F.; Zhang, M.T.; Hu, Z.R. A new absorbent by modifying walnut shell for the removal of anionic dye: Kinetic and thermodynamic studies. *Bioresour. Technol.* **2014**, *163*, 199–205. [CrossRef]

40. Yi, C.; Liao, Q.; Deng, W.; Huang, Y.; Mao, J.; Zhang, B.; Wu, G. The preparation of amorphous TiO_2 doped with cationic S and its application to the degradation of DCFs under visible light irradiation. *Sci. Total Environ.* **2019**, *684*, 527–536. [CrossRef]

41. Murgolo, S.; Moreira, I.S.; Piccirillo, C.; Castro, P.M.L.; Ventrella, G.; Cocozza, C.; Mascolo, G. Photocatalytic Degradation of Diclofenac by Hydroxyapatite-TiO_2 Composite Material: Identification of Transformation Products and Assessment of Toxicity. *Materials* **2018**, *11*, 1779. [CrossRef] [PubMed]

42. Liu, S.; Zhao, X.; Zeng, H.; Wang, Y.; Qiao, M.; Guan, W. Enhancement of photoelectrocatalytic degradation of diclofenac with persulfate activated by Cu cathode. *Chem. Eng. J.* **2017**, *320*, 168–177. [CrossRef]

43. Cheng, X.; Liu, H.; Chen, Q.; Li, J.; Wang, P. Preparation and characterization of palladium nano-crystallite decorated TiO2 nano-tubes photoelectrode and its enhanced photocatalytic efficiency for degradation of diclofenac. *J. Hazard. Mater.* **2013**, *254*, 141–148. [CrossRef] [PubMed]

44. Hartmann, J.; Bartels, P.; Mau, U.; Witter, M.; Tuempling, W.V.; Hofmann, J.; Nietzschmann, E. Degradation of the drug diclofenac in water by sonolysis in presence of catalysts. *Chemosphere* **2008**, *70*, 453–461. [CrossRef] [PubMed]